How to cite: *Angew. Chem. Int. Ed.* **2022,** *61,* e202202330
International Edition: doi.org/10.1002/anie.202202330
German Edition: doi.org/10.1002/ange.202202330

CO_2 Hydrogenation

In Situ Spectroscopic Characterization and Theoretical Calculations Identify Partially Reduced ZnO_{1-x}/Cu Interfaces for Methanol Synthesis from CO_2

Xinyu Liu[+], Jie Luo[+], Hengwei Wang[+], Li Huang[+], Shasha Wang, Shang Li, Zhihu Sun, Fanfei Sun, Zheng Jiang, Shiqiang Wei, Wei-Xue Li,* and Junling Lu**

Abstract: The active site of the industrial Cu/ZnO/Al_2O_3 catalyst used in CO_2 hydrogenation to methanol has been debated for decades. Grand challenges remain in the characterization of structure, composition, and chemical state, both microscopically and spectroscopically, and complete theoretical calculations are limited when it comes to describing the intrinsic activity of the catalyst over the diverse range of structures that emerge under realistic conditions. Here a series of inverse model catalysts of ZnO on copper hydroxide were prepared where the size of ZnO was precisely tuned from atomically dispersed species to nanoparticles using atomic layer deposition. ZnO decoration boosted methanol formation to a rate of 877 $g_{MeOH}\,kg_{cat}^{-1}\,h^{-1}$ with ≈80 % selectivity at 493 K. High pressure in situ X-ray absorption spectroscopy demonstrated that the atomically dispersed ZnO species are prone to aggregate at oxygen-deficient ZnO ensembles instead of forming CuZn metal alloys. By modeling various potential active structures, density functional theory calculations and microkinetic simulations revealed that ZnO/Cu interfaces with oxygen vacancies, rather than stoichiometric interfaces, Cu and CuZn alloys were essential to catalytic activation.

Introduction

As the rapid increase in global energy demand, enormous emission of carbon dioxide (CO_2) from consumptions of fossil energy resources (e.g. around 34 gigatonnes in 2020) has become a serious worldwide concern for global climate changes owing to the greenhouse effect.[1] Converting CO_2 into valuable chemicals is one desired approach to alleviate the dilemma.[2] Direct catalytic hydrogenation of CO_2 to methanol using green hydrogen originated from renewable energy sources, so-called "liquid sunshine",[1b,3] is particularly promising, as methanol is not only a viable alternative fuel but also a key feedstock in C1 chemistry to produce value-added chemicals such as acetic acid, formaldehyde, and olefins, so-called "methanol economy".[4] Among various catalysts developed so far,[5] the industrial Cu/ZnO/Al_2O_3 catalyst, which has been utilized for more than 50 years for methanol synthesis, is still among the most active ones, and has attracted the most attentions.[6]

Atomic-level understanding of the nature of active sites and the reaction mechanism is of essential importance to design an advanced catalyst with high methanol selectivity and yield. Regarding the industrial Cu/ZnO/Al_2O_3 catalyst in methanol synthesis, the Cu component is widely believed to be metallic Cu^0 during CO_2 hydrogenation;[6a,7] Al_2O_3 is suggested to be a structural promoter to prevent Cu and ZnO particles from sintering by physical spacing.[8] The Zn species were found to synergize strongly with Cu and promote the hydrogenation activity greatly.[9] However, the nature of active sites regarding the active phase of Zn has been heavily debated for decades, metallic Zn^0 in the form of CuZn alloys[6a,d,9b,10] and oxidative $Zn^{\delta+}$ species by forming ZnO/Cu interfaces[11,12] have been both proposed.

The aforementioned grand challenges in identification of the active phase of Zn could stem from i) very limited in situ/operando characterization techniques available for the Cu/ZnO/Al_2O_3 catalyst typically operated at above 473 K and 5 MPa; ii) challenging electron microscopic characterization owing to the close atomic weights of Zn and Cu; and iii) a fact which might have been neglected, that only a very small fraction of Zn species is in close contact with Cu^0 in the complex Cu/ZnO/Al_2O_3 industrial catalyst (Scheme 1a), which could further imped in situ/operando spectroscopic characterization significantly. Moreover, there is also lack of

[*] X. Liu,[+] J. Luo,[+] Dr. H. Wang,[+] Dr. S. Wang, S. Li, Prof. W.-X. Li, Prof. J. Lu
Department of Chemical Physics, Hefei National Laboratory for Physical Sciences at the Microscale, Key Laboratory of Surface and Interface Chemistry and Energy Catalysis of Anhui Higher Education Institutes, University of Science and Technology of China
Hefei, 230026 (China)
E-mail: wxli70@ustc.edu.cn
junling@ustc.edu.cn

Dr. L. Huang,[+] Prof. Z. Sun, Prof. S. Wei
National Synchrotron Radiation Laboratory,
University of Science and Technology of China
Hefei, 230029 (China)
E-mail: sqwei@ustc.edu.cn

Dr. F. Sun, Prof. Z. Jiang
Shanghai Advanced Research Institute, Chinese Academy of Science, China Shanghai Synchrotron Radiation Facility,
Zhangjiang National Laboratory
Shanghai, 201204 (China)

[+] These authors contributed equally to this work.

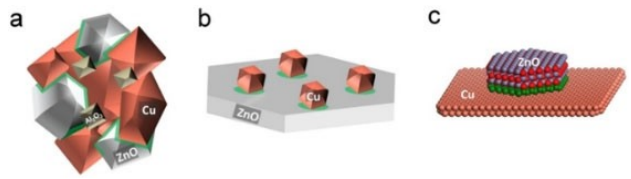

Scheme 1. a) A model of the industrial $Cu/ZnO/Al_2O_3$ catalyst, which consists of randomly packed Cu and ZnO nanocrystals and structural promoters, eg. Al_2O_3. b) A model of supported Cu/ZnO model catalysts. c) A model of ZnO/Cu inverse model catalysts. The fraction of proximate Zn species in these three types of catalyst systems are highlighted in green.

complete theoretical calculations and microkinetic simulations of all structure motifs observed to examine the reaction network in detail including both the formate pathway and the pathway of reverse water gas shift (RWGS) followed by CO hydrogenation.[11c,13]

Compared to industrial $Cu/ZnO/Al_2O_3$ and Cu/ZnO model catalysts (Scheme 1b), inverse ZnO/Cu model catalysts (Cu-supported ZnO catalysts) have much higher fraction of Zn species adjacent to Cu, which could be beneficial for spectroscopic characterization (Scheme 1c).[14] Particularly, fabrication of highly dispersed Zn species on copper-based substrates could be highly desirable for investigation of the structure evolution of Zn species under reaction conditions.

In this work, we precisely fabricated ZnO with tunable dispersions from isolated species or tiny aggregates to large ensembles, and to large islands or continuous films on $Cu(OH)_2$ nanowires (NWs) using atomic layer deposition (ALD) (see Figure 1a), a technique that relies on alternative self-limiting molecular surface reactions.[14,15] In the CO_2 hydrogenation reaction, the optimized inverse ZnO/Cu catalyst exhibited an excellent space-time-yield (STY) of methanol production of 877 $g_{MeOH}\,kg^{-1}\,h^{-1}$ along with a selectivity of $\approx$80 % at 493 K, up to 274 times higher than the Cu itself, comparable to state-of-the-art $Cu/ZnO/Al_2O_3$ catalyst, manifesting the remarkable promotion by addition of Zn. In situ X-ray absorption spectroscopy (XAS) investigated the structural evolution of atomically dispersed ZnO on $Cu(OH)_2$ during CO_2 hydrogenation under high pressures and showed that the Zn species tended to form oxygen-deficient ZnO aggregates, rather than CuZn alloys. Density functional theory (DFT) and microkinetic simulations further revealed that oxygen-vacant ZnO_{1-x}/Cu interfaces have a much higher intrinsic activity for methanol production than Cu alone, CuZn alloy and stoichiometric oxygen fully terminated ZnO/Cu interfaces, where methanol is formed preferentially via the formate pathway, rather than the RWGS reaction followed by CO hydrogenation.

Results and Discussion

Catalyst Synthesis and Structure Characterization

Compared to CuO nanorods and Cu nanocrystals (Figure S1), $Cu(OH)_2$ NWs with a high density of surface hydroxyls for ALD nucleation, were selected as the starting material to synthesize the inverse xZnO/$Cu(OH)_2$ binary catalysts (x denotes the number of ZnO ALD cycles, Figure 1a, Figures S2, S3 and Tables S1, S2). High-resolution transmission electron microscopy (HR-TEM) illustrated that ZnO lattice fringes were barely presented in the 1 ZnO/$Cu(OH)_2$ sample (Figure 1b), suggesting the ZnO species after one cycle of ZnO ALD were highly dispersed. After 3 ZnO ALD cycles, according to Fast Fourier Transforms (FFTs) and Inverse FFTs (IFFTs) (Figure S2), large ZnO ensembles with crystalline size up to 2–3 nm appeared with lattice fringes of 0.245 and 0.264 nm, assigned to hexagonal ZnO (10–11) and (0002) plane (JCPDS #36-1451), respectively (Figure 1c). Further increasing the number of ALD cycles to 12 resulted in the formation of a continuous ZnO film, as confirmed by scanning transmission electron microscopy-energy dispersive spectroscopy (STEM-EDS) mapping and cross line scan analysis (Figures 1d, e). Scanning electron microscope (SEM) measurements showed that the diameters of xZnO/$Cu(OH)_2$ increased linearly from 11.9 $\pm$ 2.4 to 19.6 $\pm$ 3.4 nm after 20 cycles of ZnO ALD, suggesting an average growth rate of $\approx$1.9 Å per cycle (Figure S3), demonstrating the precise control of ZnO species by ALD.

Raman spectroscopy measurements showed that compared to bare $Cu(OH)_2$ NWs with three characteristic peaks of Cu–O vibrations at 288, 448, and 488 cm^{-1} (Figure 1f),[16] the spectrum of 1 ZnO/$Cu(OH)_2$ remained nearly intact, implying the high dispersion of ZnO species, in a good agreement with the HR-TEM (Figure 1b) and XRD results (Figure S4). A new broad band centered at $\approx$580 cm^{-1} appeared on 2 ZnO/$Cu(OH)_2$, which developed further as increasing the number of ZnO ALD cycles. This band is assigned to the E_1(LO) mode of ZnO vibrations related with lattice defects, indicating the formation of ZnO ensembles.[17]

X-ray absorption near-edge structure (XANES) spectra of x ZnO/$Cu(OH)_2$ showed a similar shape and position of absorption edges with that of ZnO reference, indicating a +2 valence state (Figure 1g). In addition, we found that the peak at 9679 eV, assigned to multiple scattering of Zn–Zn shells according to ZnO reference,[18] were barely observed in 1 ZnO/$Cu(OH)_2$, but gradually developed in intensity as increase of ZnO ALD cycles. Meanwhile, Fourier transforms (FTs) of the extended X-ray absorption fine structure (EXAFS) also showed that along with the first Zn–O shell at 1.56 Å, the secondary shell of Zn–O–Zn coordination at 2.88 Å was absent on 1 ZnO/$Cu(OH)_2$, but gradually developed as increasing ZnO ALD cycles (Figure 1h and Figure S5). The Zn–O coordination number (CN) was about 4.5 for all x ZnO/$Cu(OH)_2$ samples; the Zn–O–Zn CNs were 0, 2.1 $\pm$ 0.6, 4.4 $\pm$ 0.8, 4.6 $\pm$ 0.8, 5.0 $\pm$ 0.8 and 6.5 $\pm$ 0.7 for 1-, 2-, 3-, 6-, 12-, and 20 ZnO/$Cu(OH)_2$, respectively (Figures S6, S7 and Table S3). These results clearly suggest the ZnO

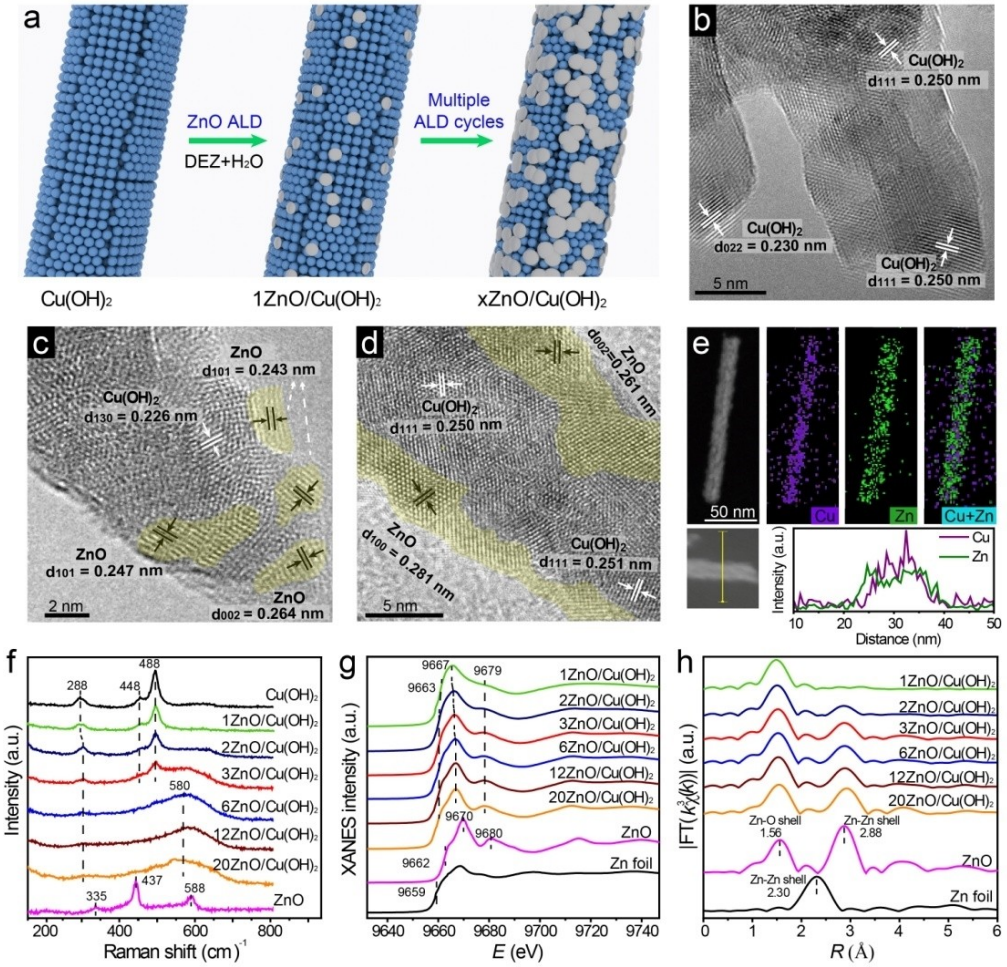

Figure 1. a) Illustration of synthesizing inverse xZnO/Cu(OH)$_2$ catalysts using ALD by alternatively exposing to diethylzinc (DEZ) and water. Representative high resolution TEM images of b) 1 ZnO/Cu(OH)$_2$, c) 3 ZnO/Cu(OH)$_2$ and d) 12 ZnO/Cu(OH)$_2$, respectively. The yellow areas in (c) and (d) highlight the ZnO islands/films. e) A representative STEM image and the EDS elemental mapping images of 12 ZnO/Cu(OH)$_2$, where Cu Kα1, Zn Kα1 and the constructed Cu + Zn signals were performed, followed by the corresponding line-scan analysis. f) Raman spectra of Cu(OH)$_2$ and a variety of xZnO/Cu(OH)$_2$ binary catalysts (x = 1, 2, 3, 6, 12, 20). The Raman spectrum of ZnO is also shown for comparison. g) Normalized XANES spectra of xZnO/Cu(OH)$_2$ binary catalysts (x = 1, 2, 3, 6, 12, 20) and references of ZnO and Zn foil at the Zn K edge and h) the corresponding k^3-weighted FT-EXAFS spectra in R-space.

species on Cu(OH)$_2$ were tuned gradually from isolated species or tiny aggregates to large ensembles, and to large islands or continuous films, in a good agreement with the HR-TEM, XRD and Raman.

Catalytic Performance

The catalytic performance of these xZnO/Cu(OH)$_2$ catalysts was evaluated in the CO_2 hydrogenation reaction with a H_2:CO_2 ratio of 3:1 at 493 K, and a pressure of 4.5 MPa. Here we noticed that Cu(OH)$_2$ was reduced to metallic Cu crystals after reduction at 493 K before reaction (Figure S8). The bare Cu(OH)$_2$ sample showed a very low methanol STY of 3.2 $g_{MeOH}\,kg_{cat}^{-1}\,h^{-1}$, and a low methanol selectivity of 7.1 % (Figure 2a,b and Tables S4). After one cycle of ZnO ALD, the 1 ZnO/Cu(OH)$_2$ sample showed a methanol STY of 654 $g_{MeOH}\,kg_{cat}^{-1}\,h^{-1}$, about 204 times higher than that of bare Cu(OH)$_2$, along with a methanol selectivity of 81 %, strongly indicating the remarkable promotion of Zn in methanol synthesis. As increasing the Zn content, the methanol STY showed a volcano-like trend on the Zn content with a maximum value as high as 877 $g_{MeOH}\,kg^{-1}\,h^{-1}$ on 3 ZnO/Cu(OH)$_2$, which is about 274 times higher than that of bare Cu(OH)$_2$; Calculation of STY based on the Cu content exhibited a similar trend on the Zn content as well (Figure S9). Therein the methanol selectivity was almost constant at ≈80 % at comparable CO_2 conversion (Figure 2b and Tables S4). We noted that the optimized 3 ZnO/Cu(OH)$_2$ catalyst was considerably better than the Cu–ZnO binary catalysts synthesized by the co-precipitation method with the same Zn content (Cu–ZnO–CP, methanol STY 669 $g_{MeOH}\,kg_{cat}^{-1}\,h^{-1}$, and methanol selectivity 74 %), and even comparable to Cu/ZnO/Al_2O_3 ternary catalysts (methanol STY 826 $g_{MeOH}\,kg_{cat}^{-1}\,h^{-1}$, and methanol selectivity 77 %). These results demonstrate the advantages of the

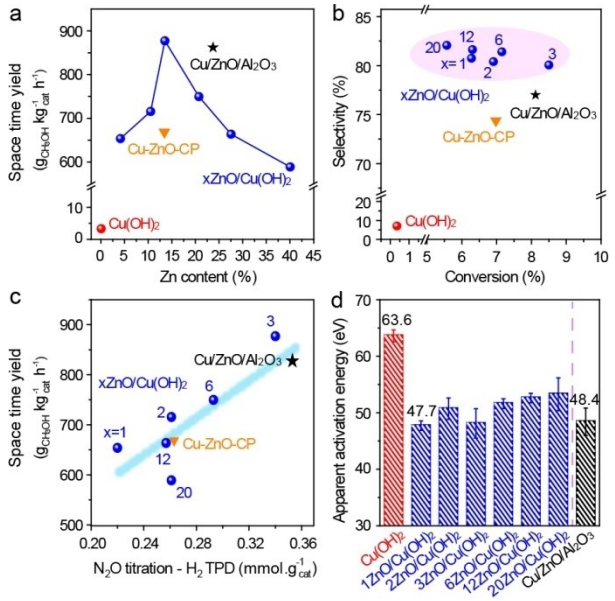

Figure 2. Catalytic performance of xZnO/Cu(OH)$_2$ (x = 1, 2, 3, 6, 12 and 20), co-precipitated Cu–ZnO and commercial Cu/ZnO/Al_2O_3 catalysts in CO_2 hydrogenation. a) Initial methanol STYs as a function of Zn contents and b) methanol selectivity as a function of CO_2 conversion at 493 K. c) The correlations between methanol STYs to the amount of oxophilic Zn sites, as determined by the surface area difference between N_2O titration and H_2-TPD. Reaction conditions: Catalyst, 50 mg; temperature, 493 K; pressure, 4.5 MPa; WHSV, 37 600 mL g^{-1} h^{-1}. d) The apparent activation energies of Cu(OH)$_2$, xZnO/Cu(OH)$_2$ and Cu/ZnO/Al_2O_3 catalysts in CO_2 hydrogenation.

ALD method in precise control over the intimacy of Cu and Zn species for activity promotion (Table S5).

To understand the nature of the active sites, temperature-programmed desorption of H_2 (H_2-TPD) and N_2O titration were performed to measure the exposed Cu surface area and integrated areas including both exposed Cu and oxophilic Zn sites due to oxygen-deficient ZnO and or metallic Zn.[10b,19] We found that the amount of sites determined by N_2O titration were all considerably larger than those by H_2-TPD over xZnO/Cu(OH)$_2$ and Cu/ZnO/Al_2O_3 catalysts (Table S6). Correlation of methanol STYs with different kinds of sites revealed that methanol STYs was approximately proportional to the amount of oxophilic Zn sites as determined by the surface area difference between N_2O titration and H_2-TPD, instead of others (Figures 2c and S10), implying that the active sites are directly related to oxophilic Zn species. Here we noticed that xZnO/Cu(OH)$_2$ model catalysts showed higher concentrations of oxophilic Zn sites than Cu–ZnO–CP and Cu/ZnO/Al_2O_3 catalysts (Figure S11), endowing these ALD inverse catalysts to exhibit a remarkable performance even with much lower Zn contents. Kinetic studies further showed that xZnO/Cu(OH)$_2$ and commercial Cu/ZnO/Al_2O_3 catalyst had a rather similar apparent reaction energy of $\approx$48 kJ mol^{-1}, which are much lower than that of the bare Cu(OH)$_2$ (63.6 kJ mol^{-1}), clarifying the remarkable promotion by Zn (Figure 2d and Figure S12). Similar apparent reaction energies also suggest that the nature of active sites in these ALD inverse catalysts are basically same with those in commercial Cu/ZnO/Al_2O_3 catalyst.

Stability tests were also carried out on 1 ZnO/Cu(OH)$_2$, 3 ZnO/Cu(OH)$_2$ and Cu/ZnO/Al_2O_3 catalysts. We found that the 1 ZnO/Cu(OH)$_2$ catalyst deactivated slowly during the first 30 h, and then became rather stable at a methanol STY of 400 g_{MeOH} kg^{-1} h^{-1} (Figure S13), indicating the possible structure changes of atomically dispersed ZnO species under reaction conditions. The 3 ZnO/Cu(OH)$_2$ catalyst with the highest methanol STY, showed a relatively better stability, reaching a methanol STY of 750 g_{MeOH} kg^{-1} h^{-1} in the stable regime, which is very close to the commercial Cu/ZnO/Al_2O_3 ternary catalyst. XRD measurements of the used ZnO/Cu(OH)$_2$ catalysts showed that the underlying Cu(OH)$_2$ NWs were reduced to metallic Cu totally after the initial 2 h of reaction, and the formed metallic Cu were further aggregates during the reaction time of 50 h on stream (Figure S14a, b). Meanwhile HR-TEM measurements also revealed that the changes of the morphology of NWs to copper nanocrystals, and in particularly, ZnO nanoparticles with a size up to $\approx$3 nm were observed in the used 1 ZnO/Cu(OH)$_2$ sample (Figure S14c–f).

In Situ XAFS Characterization of 1 ZnO/Cu(OH)$_2$

Since it is generally believed that metallic Cu is the active phase of Cu component for methanol synthesis according to extensive literature,[4d,7,20] here we mainly focused on the structure evaluation of Zn-involved species under reaction conditions using in situ XAFS characterization. As discussed previously, the nature of active sites are basically same in all xZnO/Cu(OH)$_2$ catalysts. The 1 ZnO/Cu(OH)$_2$ catalyst contained atomically dispersed ZnO species in the as-prepared sample (Figure 1), and exhibited a reasonably high methanol STY, thus providing an excellent platform for in situ spectroscopic characterization of Zn species under reaction conditions.

In situ XAFS investigation of the 1 ZnO/Cu(OH)$_2$ catalyst under CO_2 hydrogenation reaction conditions was carried at the Zn K edge under a pressure of 0.8 MPa (a highest pressure we can reach so far). Both in situ XANES spectra and FTs of EXAFS showed that the ZnO species remained atomically dispersed at below 393 K (Figure 3a, b and Figure S15). Increasing the reaction temperature to 433 K, isolated ZnO species appeared to aggregate to small ensembles as indicated by the appearance of the new Zn–O–Zn multiple scattering peak at 9679 eV in the XANES spectrum, and the Zn–O–Zn coordination peak at 2.88 Å in the EXAFS curve in the real (R) space. Further increase the reaction temperature to 493 K, ZnO aggregations became more pronounced. Meanwhile, we noticed that the shape and the position of absorption edges of the XANES curve resembled that of ZnO reference well. These results suggest that Zn remained at the +2 valence state at the reaction temperature of 493 K. To further track the changes in the XANES spectra of 1 ZnO/Cu(OH)$_2$ as increasing temperature, the first derivatives of the XANES spectra were shown in Figure 3c. We observed that the

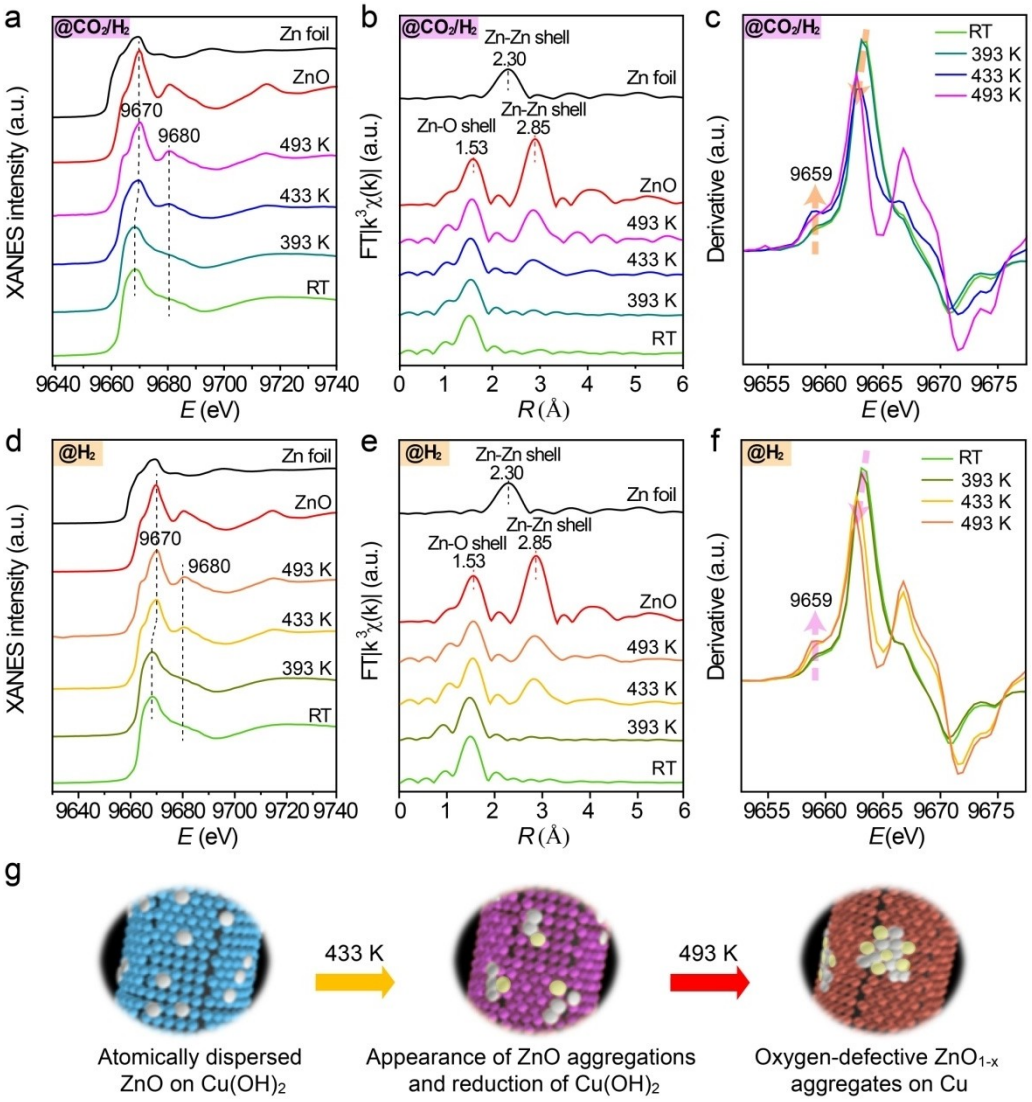

Figure 3. In situ XAFS investigation of the 1 ZnO/$Cu(OH)_2$ inverse catalyst under the conditions of CO_2 hydrogenation reaction and H_2 reduction at the Zn *K* edge. a) Normalized XANES spectra and b) FTs of EXAFS spectra of 1 ZnO/$Cu(OH)_2$ during CO_2 hydrogenation under a pressure of 0.8 MPa at different temperatures. The spectra of ZnO and Zn foil references are also shown for comparison. c) First derivative of the Zn *K* edge spectra of the 1 ZnO/$Cu(OH)_2$ inverse catalyst during CO_2 hydrogenation at different temperatures. d) Normalized XANES spectra and e) FTs of EXAFS spectra of 1 ZnO/$Cu(OH)_2$ during H_2 reduction at difference temperatures and a pressure of 0.1 MPa. f) First derivative of the Zn *K* edge spectra of the 1 ZnO/$Cu(OH)_2$ inverse catalyst during H_2 reduction at different temperatures. g) Schematic illustration of structure evolution of isolated ZnO to small aggregates as increasing temperature during either CO_2 hydrogenation reaction or H_2 reduction. The balls in white, light yellow, light blue, purple and brown represent ZnO, oxygen-defective ZnO_{1-x}, $Cu(OH)_2$, partially reduced $Cu(OH)_2$, and metallic Cu, respectively.

absorption edge at 9663 eV (1*s*–4*p* transition) went through a small shift toward low energy as increasing reaction temperature. Additionally, a weak pre-edge peak at 9659 eV assigned to defect-induced local interferences according to literature,[21] also appeared. Therefore, these results might indicate the presence of considerable amount of oxygen vacancies in ZnO under reaction conditions. Indeed, XPS measurements confirmed the presence of oxygen vacancies in the ZnO of 1 ZnO/$Cu(OH)_2$ catalyst after reaction gas treatment (Figure S16).

We also investigated the structure evolution of ZnO species during reduction in 10 % H_2 in He using in situ XAFS at the Zn *K* edge. Interestingly, we observed very similar structural changes, the Zn species remained atomically dispersed under 393 K, and started aggregating at above 433 K (Figure 3d–f), which might be induced by the $Cu(OH)_2$ dehydration (Figure S17). While no further aggregations were found at 493 K. The above structure evolution of Zn species in the conditions of either CO_2 hydrogenation or H_2 reduction is described in Figure 3g.

Least-squares EXAFS curve-fittings showed that the Zn–O coordination number remained nearly constant at 4.3 regardless of temperatures and conditions (Table S7, Figures S18, S19). While the Zn–O–Zn coordination was 0, 0, 3.5 ± 0.5 and 7.0 ± 0.8 after exposing the 1 ZnO/$Cu(OH)_2$ to the reaction gases at RT, 393, 433, and 493 K, respectively.

Considerable increase of Zn–O–Zn coordination clearly manifests the formation of ZnO nanoparticles during reactions at 493 K and a pressure of 0.8 MPa. However, no feature of Zn–Cu or Zn–Zn coordination peaks was observed, thus the formation of the metallic Zn and CuZn alloy was excluded under our conditions. These results are in line with the previous report, where Zn^0 was not found at a reduction temperature below 510 K in XAFS measurements.[7,22] We varied the pressure, while no obvious features were found related to the formation of metallic Zn (Figures S20, S21). Given the remarkable activity promotion by Zn in Figure 2, our results clearly suggest that Cu–ZnO interfaces can be the catalytic active sites in CO_2 hydrogenation to methanol as discussed below.

Theoretical Insight of the Nature of Active Sites

To reveal the origin of the above remarkable promotion by Zn species, comprehensive DFT calculations and microkinetic simulations were carried out. Here Cu(111) surface, CuZn (211) alloy surfaces, stoichiometric ZnO/Cu(111) interfaces and partially reduced oxygen-vacant ZnO_{1-x}/Cu(111) interfaces, were used to model various potential active sites (Figure 4). Given the experimental observation of layered graphic ZnO structure (Figure S22),[12a,23] one graphic layer of ZnO was constructed on Cu(111) to simulate the metal-oxide interface, where ZnO/Cu(111) interface represents the stoichiometric oxygen fully terminated edge along the perimeter of the ZnO islands. To reveal whether the oxygen-deficient ZnO as observed by in situ XAFS (Figure 3c), N_2O titration and H_2-TPD (Figure 2c) plays a certain role or not, oxygen-vacant ZnO_{1-x}/Cu interface by removing one third interfacial oxygen was also calculated. For the reaction network, methanol can be produced via either the formate pathway, or the pathway of RWGS followed by CO hydrogenation. Both pathways were examined for the four structure motifs considered, which are essential for identification of the active sites and corresponding mechanism.

We start from Cu(111), and the optimized potential energy surfaces (PES) for formate pathway is shown in

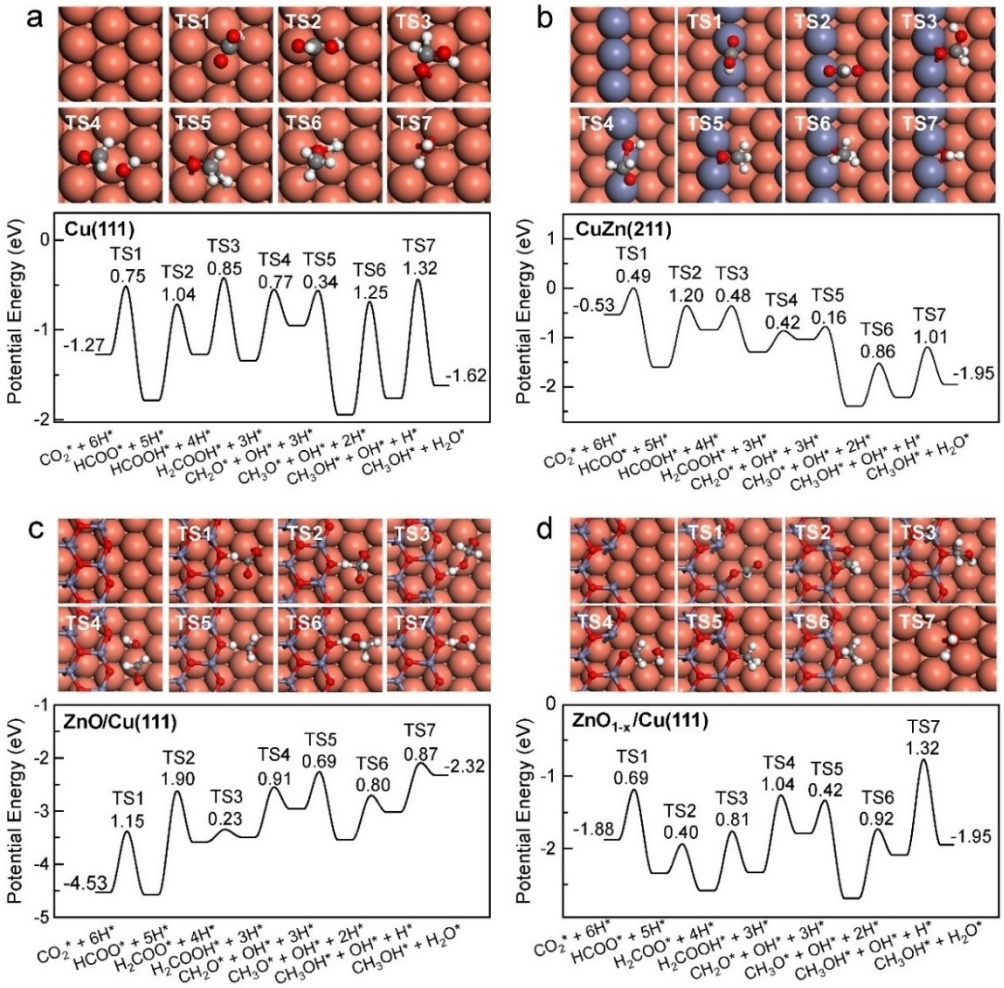

Figure 4. Reaction energy profiles of CO_2 hydrogenation on a) Cu(111), b) CuZn(211), c) ZnO/Cu(111) and d) ZnO_{1-x}/Cu(111) in the favorable formate pathway, where the top views of transition states (TS) configurations and corresponding barriers are indicated. The brown, red, gray, black and white balls represent Cu, O, Zn, C and H atoms, respectively. The energy reference zero corresponds to the energy of H_2 and CO_2 in gas phase.

Figure 4a, Figure S23 and Table S8. The dissociated H* atom (* denotes surface species hereafter) first attacks the C atom of the adsorbed CO_2* to form HCOO* with an exothermic reaction energy of 0.51 eV and a barrier of 0.75 eV. In the followings, H* attacks the O atom of HCOO* to form HCOOH* with an endothermic energy of 0.51 eV and a considerable barrier of 1.04 eV, then attacks the C atom to form H_2COOH*. Next, the formed H_2COOH* decomposes to H_2CO* and OH*, which remains endothermic by 0.39 eV with a barrier of 0.77 eV. Sequential addition of H* to CH_2O* forms CH_3O* and then the second H* addition to form CH_3OH* by overcoming a barrier of 1.25 eV. Meanwhile, reaction of OH* with H* on Cu(111) is also kinetic demanding with a barrier of 1.32 eV. In the pathway of RWGS followed by CO hydrogenation, addition of H* to CO_2* to form COOH* has a considerably high barrier of 1.71 eV and an endothermic energy of 0.35 eV (Figure S24 and Table S9), thus would have no contribution to the methanol formation. Preference of the formate pathway on Cu surfaces found here are in line with literature.[24]

On CuZn(211) alloy surface, H* atom binding (−0.05 eV) is rather weak (Figure 4b and Table S10). In the formate pathway, the H* addition to HCOOH* to form H_2COOH* is highly endothermic by 0.75 eV with a barrier of 1.2 eV (Figures 4b and Figure S25). Whereas for the RWGS pathway, hydrogenation of CO_2* to COOH* has a considerable barrier of 1.28 eV as well (Figure S24). The dominance of the formate pathway on CuZn(211) are also in line with the works by Studt et al.[25]

We then turn to the ZnO/Cu(111) interfaces where the stoichiometric ZnO edge fully terminated by oxygen was studied first, although theoretical calculations on such interface was rarely mentioned. Compared to the weak dissociative H binding on Cu(111) (−0.18 eV), H dissociative adsorption to the edge oxygen is significantly enhanced to −0.75 eV (Table S10). Too strong binding of H*, downshifts dramatically the overall PES and makes subsequent hydrogenation via the formate pathway endothermic and kinetically limited (Figures 4c and S26). Specifically, the H* attack the C atom of HCOO* to form H_2COO* is endothermic by 0.99 eV along with a barrier of 1.90 eV. Such strong binding also prevents the addition of H* to O of CO_2, which makes the RWGS pathway unlikely. Such high barrier and unfavorable reaction energetics suggests that the ZnO/Cu(111) interface with full oxygen termination and/or the hydroxylated ZnO/Cu(111) interface are inactive for the methanol formation.

In contrast, our calculations show that the oxygen-vacant ZnO_{1-x}/Cu(111) interfaces is highly active for methanol synthesis via the formate pathway. In this case, the exposed Zn cation binds CO_2 considerably stronger than H* (−0.56 vs 0.16 eV) (Table S10 and Figure S28), and H* atom would bind the Cu sites nearby with a binding energy of −0.22 eV. Bader charges analysis also showed that CO_2* at ZnO_{1-x}/Cu(111) has a considerably larger Bader charge of $-1.06|e|$ than that of H* $-0.30|e|$. This agrees with the literature excellently, where CO_2 was found to preferentially bind to the Zn sites at the ZnO/Cu interfaces.[11c,26] We note that the oxygen fully terminated ZnO/Cu interface studied above doesn't bind CO_2, and CO_2 adsorbs at the Cu sites nearby with a weaker adsorption energy of −0.19 eV. These together downshifts the overall PES in an optimum position, as indicated in Figure 4d. This H* atom is very active for subsequent hydrogenation to CO_2* to form HCOO*, H_2COO* and H_2COOH*, with favorable reaction energies of −0.46, −0.24 and 0.25 eV and modest barriers of 0.69, 0.40 and 0.81 eV (Figure S27). Decomposition of H_2COOH* to CH_2O* and OH* is endothermic by 0.54 eV and a relatively high barrier of 1.04 eV. Here decomposed CH_2O* and OH* are located at the ZnO_{1-x}/Cu(111) interface and the Cu sites nearby, respectively. Next, sequential H* additions to CH_2O* to form CH_3O* and CH_3OH* also exhibit relatively low barriers of only 0.42 and 0.92 eV, compared to 1.25 eV for the final hydrogenation to form methanol on Cu(111). OH* formed at Cu(111) reacts with H* on Cu(111) to form water. As shown in Figure 4d for the ZnO_{1-x}/Cu(111) interfaces, the overall PES is energetically more favorable than that of ZnO/Cu(111), and high catalytic activity is expected. For the RWGS pathway, corresponding reactivity is kinetically less favorable, where H* addition to CO_2* to form COOH* and the subsequent C–O bond cleavage to form CO* and OH* have considerable barrier of 0.97 and 1.23 eV, respectively (Figure S24). These are already much higher than the first two steps in direct hydrogenation studied above, indicating a lower overall activity than the formate path, which is confirmed below by explicit kinetics simulation.

To quantify the intrinsic activity on the four structural motifs constructed, we conducted microkinetic simulations under the conditions of $CO_2:H_2=1:3$ at a pressure of 4.5 MPa in the temperature range of 400–670 K, according to the experimental conditions. Here all reaction pathways including CO_2 hydrogenation to methanol via formate pathway, or RWGS followed by CO hydrogenation were simultaneously included in the kinetic calculations. In line with above PES, the kinetics calculations show that the formate pathway is orders of magnitude more active than the RWGS followed by CO hydrogenation, regardless the various structural motifs considered (Figure S29). Moreover, the activity for the methanol formation on oxygen-vacant ZnO_{1-x}/Cu(111) interface is much more active than Cu(111), CuZn(211) alloy and ZnO/Cu(111) interface in the entire temperature range considered (Figure 5a). CuZn(211) alloy becomes more active than Cu(111) only at high temperatures above 590 K. The ZnO/Cu(111) interface has the poorest and negligible activity. In addition, the formation rate of methanol over oxygen-vacant ZnO_{1-x}/Cu(111) interface increases as increasing the reaction temperature (Figure S29). Moreover, the formation rate on ZnO_{1-x}/Cu(111) was exclusively higher than that of Cu(111), in good agreement with the trend behavior found in measurements. Partially reduced ZnO_{1-x}/Cu(111) interface could be the catalytic active sites in methanol synthesis, accounting for the remarkable Zn promotion on Cu in Figure 2. This is consistent well with the experimental results of in situ XAFS (Figure 3c) and XPS (Figure S16) where a considerable oxygen deficiencies were observed on the 1 ZnO/Cu(OH)$_2$

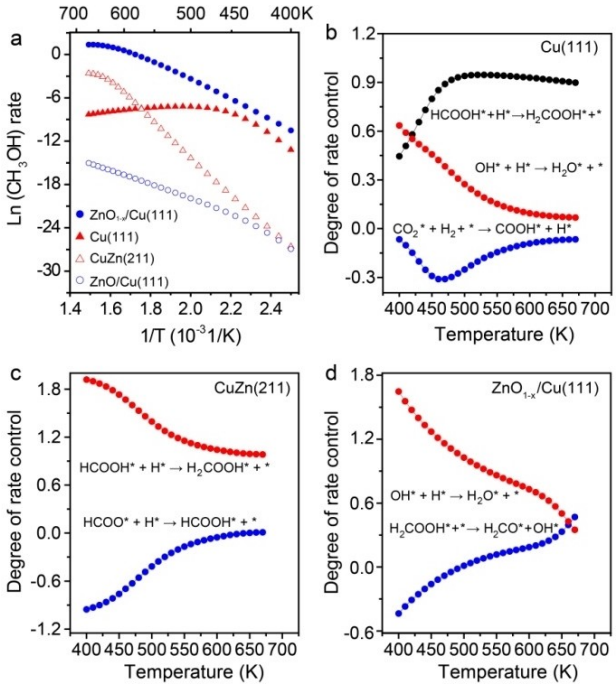

Figure 5. Microkinetic simulations of CO_2 hydrogenation at a pressure of 4.5 MPa in the temperature range of 400–670 K with a ratio of $CO_2:H_2=1:3$. a) Activity and of CO_2 hydrogenation to methanol on Cu(111), CuZn(211), ZnO/Cu(111) and ZnO_{1-x}/Cu(111); Corresponding DRC for b) Cu(111), c) CuZn(211), and d) ZnO_{1-x}/Cu(111), respectively.

catalyst under reaction conditions. Comparing to the previous calculations on small ZnO_x clusters,[11c,26] here we investigated the extended ZnO stripes which is more appropriate and relevant to experiments (Figure S22). We considered both stoichiometric ZnO/Cu and oxygen-vacant ZnO_{1-x}/Cu interfaces and provided the first evidence that the former one is not active, and the active interface structure is related to the latter one, agreeing perfectly with the approximately linear correlation between methanol STYs and the amount of oxophilic Zn sites (Figure 2c).

Furthermore, the DRC analysis as a function of temperature is performed to understand the importance of the elementary steps to activity. It can be found that on Cu(111) (Figure 5b), the activity is mostly limited by HCOOH* hydrogenation, and followed by water formation. Low rate for the HCOOH* hydrogenation comes in a large extent from the HCOOH* formation that is endothermic by 0.51 eV. On CuZn(211) surfaces (Figure 5c), the HCOOH* hydrogenation as the rate-determining step was even strengthened. On ZnO/Cu(111) (Figure S30), the undisputed rate-determining step is HCOO* hydrogenation with a huge barrier of 1.9 eV, due to the strong binding of H atom at the ZnO/Cu(111) interface. On ZnO_{1-x}/Cu(111) (Figure 5d), hydrogenation to CO_2 becomes facile for the optimum binding of H atom and improved adsorption of CO_2 at the ZnO_{1-x}/Cu(111) interface, and the water formation on the Cu domain turns out to be the rate-determining step.

Above theoretical calculations implies that the partially reduced ZnO_{1-x}/Cu(111) interfaces with exposed Zn cation is the most active site and CO_2 hydrogenation proceeds preferentially via the formate pathways. These theoretical results are further supported by in situ DRIFTS measurements (Figure S31), where the formation of formate species at 1587 and 1340 cm^{-1}, assigned to the asymmetric and symmetric O–C–O stretching vibrations, were observed along with the methoxy group at 1050 cm^{-1} during exposure of 1 ZnO/Cu(OH)$_2$ to CO_2/H_2 mixture gas.[27] Moreover, switching the gas to H_2, the intensities of all these features decreased.

Conclusion

In summary, we have successfully synthesized a series of inverse model catalysts of ZnO/Cu(OH)$_2$ with the size of ZnO precisely tuned from atomically dispersed species to nanoparticles using ALD. In the CO_2 hydrogenation reaction, we demonstrated that the ZnO decoration prompted the methanol STY up to 274 times higher than the copper itself by largely improving both activity and selectivity. High-pressure in situ XAFS revealed that under reaction conditions, atomically dispersed ZnO species tended to aggregate to oxygen-deficient ZnO ensembles, instead of forming CuZn alloy. DFT calculations and microkinetic simulations further revealed that oxygen-vacant ZnO_{1-x}/Cu(111) interfaces show a much higher activity than Cu(111), CuZn(211) alloys and stoichiometric ZnO/Cu(111) interfaces, where the reaction proceeds preferentially via the formate pathway owing to the optimum binding to H atom and improved adsorption of CO_2. Comparing to recent experimental observation of transformation of CuZn alloy to zinc oxide under reaction conditions and previous theoretical calculations on small ZnO_x clusters, these results provided the first evidence that oxygen-vacant ZnO_{1-x}/Cu interface, rather than stoichiometric ZnO/Cu, is essential for remarkable activity promotion. Finally, we might speculate that development of a strategy to optimize ZnO/Cu interfaces while maintaining the partial reduction of ZnO at low temperatures could be highly desirable for enhancing methanol production.

Acknowledgements

This work was supported by National Key R&D Program of China (2021YFA1502802), the National Natural Science Foundation of China (22025205, 91645202, 91845203, 91945302), the Dalian National Laboratory For Clean Energy (DNL) Cooperation Fund (DNL201907, DNL201920), the Fundamental Research Funds for the Central Universities (WK2060030029), Chinese Academy of Sciences (QYZDJ-SSW-SLH054), K. C. Wong Education (GJTD-2020-15), Users with Excellence Program of Hefei Science Center CAS (2019HSC-UE016), the China Postdoctoral Science Foundation (2021M693057), and the National Synchrotron Radiation Laboratory (KY9990000158) from

the University of Science and Technology of China. The authors also gratefully thank the BL14W1 beamline at the Shanghai Synchrotron Radiation Facility (SSRF), China, and Supercomputing Center of University of Science and Technology of China.

Conflict of Interest

The authors declare no competing financial interests.

Data Availability Statement

The data that support the findings of this study are available from the corresponding author upon reasonable request.

Keywords: Atomic Layer Deposition · CO_2 Hydrogenation · First-principles microkinetics · Metal-Oxide Interface · In Situ XAFS

[1] a) C. Le Quéré, G. P. Peters, P. Friedlingstein, R. M. Andrew, J. G. Canadell, S. J. Davis, R. B. Jackson, M. W. Jones, *Nat. Clim. Change* **2021**, *11*, 197–199; b) C. F. Shih, Z. Tao, J. Li, C. Bai, *Joule* **2018**, *2*, 1925–1949; c) D. Xu, Y. Wang, M. Ding, X. Hong, G. Liu, S. Tsang, *Chem* **2021**, *7*, 849–881.

[2] a) X. Lim, *Nature* **2015**, *526*, 628–630; b) E. Gomez, X. Nie, H. L. Ji, Z. Xie, J. G. Chen, *J. Am. Chem. Soc.* **2019**, *141*, 17771–17782; c) B. M. Tackett, H. L. Ji, J. G. Chen, *Acc. Chem. Res.* **2020**, *53*, 1535–1544; d) X. Wang, P. J. Ramirez, W. Liao, J. A. Rodriguez, P. Liu, *J. Am. Chem. Soc.* **2021**, *143*, 13103–13112.

[3] G. A. Olah, G. K. Surya Prakash, *Beyond Oil and Gas:The Methanol Economy*, Wiley-VCH, Weinheim, **2011**.

[4] a) A. Goeppert, M. Czaun, J.-P. Jones, G. K. Surya Prakash, G. A. Olah, *Chem. Soc. Rev.* **2014**, *43*, 7995–8048; b) A. Álvarez, A. Bansode, A. Urakawa, A. V. Bavykina, T. A. Wezendonk, M. Makkee, J. Gascon, F. Kapteijn, *Chem. Rev.* **2017**, *117*, 9804–9838; c) X. Jiang, X. Nie, X. Guo, C. Song, J. G. Chen, *Chem. Rev.* **2020**, *120*, 7984–8034; d) J. Zhong, X. Yang, Z. Wu, B. Liang, Y. Huang, T. Zhang, *Chem. Soc. Rev.* **2020**, *49*, 1385–1413.

[5] a) F. Studt, I. Sharafutdinov, F. Abild-Pedersen, C. F. Elkjaer, J. S. Hummelshoj, S. Dahl, I. Chorkendorff, J. K. Norskov, *Nat. Chem.* **2014**, *6*, 320–324; b) J. Graciani, K. Mudiyanselage, F. Xu, A. E. Baber, J. Evans, S. D. Senanayake, D. J. Stacchiola, P. Liu, J. Hrbek, J. F. Sanz, *Science* **2014**, *345*, 546–550; c) J. Wang, G. Li, Z. Li, C. Tang, Z. Feng, H. An, H. Liu, T. Liu, C. Li, *Sci. Adv.* **2017**, *3*, e1701290; d) K. Larmier, W.-C. Liao, S. Tada, E. Lam, R. Verel, A. Bansode, A. Urakawa, A. Comas-Vives, C. Copéret, *Angew. Chem. Int. Ed.* **2017**, *56*, 2318–2323; *Angew. Chem.* **2017**, *129*, 2358–2363; e) S. Kattel, B. Yan, Y. Yang, J. G. Chen, P. Liu, *J. Am. Chem. Soc.* **2016**, *138*, 12440–12450; f) H. Bahruji, M. Bowker, G. Hutchings, N. Dimitratos, P. Wells, E. Gibson, W. Jones, C. Brookes, D. Morgan, G. Lalev, *J. Catal.* **2016**, *343*, 133–146.

[6] a) M. Behrens, F. Studt, I. Kasatkin, S. Kühl, M. Hävecker, F. Abild-Pedersen, S. Zander, F. Girgsdies, P. Kurr, B.-L. Kniep, *Science* **2012**, *336*, 893–897; b) M. D. Porosoff, B. Yan, J. G. Chen, *Energy Environ. Sci.* **2016**, *9*, 62–73; c) E. V. Kondratenko, G. Mul, J. Baltrusaitis, G. O. Larrazábal, J. Pérez-Ramírez, *Energy Environ. Sci.* **2013**, *6*, 3112–3135; d) S. Kuld, M. Thorhauge, H. Falsig, C. F. Elkjær, S. Helveg, I. Chorkendorff, J. Sehested, *Science* **2016**, *352*, 969–974.

[7] R. van den Berg, G. Prieto, G. Korpershoek, L. I. van der Wal, A. J. van Bunningen, S. Laegsgaard-Jorgensen, P. E. de Jongh, K. P. de Jong, *Nat. Commun.* **2016**, *7*, 13057.

[8] a) M. Behrens, S. Zander, P. Kurr, N. Jacobsen, J. Senker, G. Koch, T. Ressler, R. W. Fischer, R. Schlögl, *J. Am. Chem. Soc.* **2013**, *135*, 6061–6068; b) T. Lunkenbein, F. Girgsdies, T. Kandemir, N. Thomas, M. Behrens, R. Schlogl, E. Frei, *Angew. Chem. Int. Ed.* **2016**, *55*, 12708–12712; *Angew. Chem.* **2016**, *128*, 12900–12904.

[9] a) J. Nakamura, I. Nakamura, T. Uchijima, Y. Kanai, T. Watanabe, M. Saito, T. Fujitani, *J. Catal.* **1996**, *160*, 65–75; b) T. Fujitani, J. Nakamura, *Catal. Lett.* **1998**, *56*, 119–124.

[10] a) Y. Choi, K. Futagami, T. Fujitani, J. Nakamura, *Appl. Catal. A* **2001**, *208*, 163–167; b) S. Kuld, C. Conradsen, P. G. Moses, I. Chorkendorff, J. Sehested, *Angew. Chem. Int. Ed.* **2014**, *53*, 5941–5945; *Angew. Chem.* **2014**, *126*, 6051–6055.

[11] a) J. Frost, *Nature* **1988**, *334*, 577–580; b) F. Liao, Y. Huang, J. Ge, W. Zheng, K. Tedsree, P. Collier, X. Hong, S. C. Tsang, *Angew. Chem. Int. Ed.* **2011**, *50*, 2162–2165; *Angew. Chem.* **2011**, *123*, 2210–2213; c) S. Kattel, P. J. Ramírez, J. G. Chen, J. A. Rodriguez, P. Liu, *Science* **2017**, *355*, 1296–1299; d) R. M. Palomino, P. J. Ramirez, Z. Liu, R. Hamlyn, I. Waluyo, M. Mahapatra, I. Orozco, A. Hunt, J. P. Simonovis, S. D. Senanayake, J. A. Rodriguez, *J. Phys. Chem. B* **2018**, *122*, 794–800; e) M. Zabilskiy, V. L. Sushkevich, D. Palagin, M. A. Newton, F. Krumeich, J. A. van Bokhoven, *Nat. Commun.* **2020**, *11*, 2409.

[12] a) T. Lunkenbein, J. Schumann, M. Behrens, R. Schlögl, M. G. Willinger, *Angew. Chem. Int. Ed.* **2015**, *54*, 4544–4548; *Angew. Chem.* **2015**, *127*, 4627–4631; b) D. Laudenschleger, H. Ruland, M. Muhler, *Nat. Commun.* **2020**, *11*, 3898.

[13] a) Q.-L. Tang, W.-T. Zou, R.-K. Huang, Q. Wang, X.-X. Duan, *Phys. Chem. Chem. Phys.* **2015**, *17*, 7317–7333; b) S. Wang, M. Jian, H. Su, W.-X. Li, *Chin. J. Chem. Phys.* **2018**, *31*, 284–290.

[14] L. Cao, W. Liu, Q. Luo, R. Yin, B. Wang, J. Weissenrieder, M. Soldemo, H. Yan, Y. Lin, Z. Sun, C. Ma, W. Zhang, S. Chen, H. Wang, Q. Guan, T. Yao, S. Wei, J. Yang, J. Lu, *Nature* **2019**, *565*, 631–635.

[15] a) B. Zhang, Y. Qin, *ACS Catal.* **2018**, *8*, 10064–10081; b) J. Lu, J. W. Elam, P. C. Stair, *Surf. Sci. Rep.* **2016**, *71*, 410–472; c) B. J. O'Neill, D. H. Jackson, J. Lee, C. Canlas, P. C. Stair, C. L. Marshall, J. W. Elam, T. F. Kuech, J. A. Dumesic, G. W. Huber, *ACS Catal.* **2015**, *5*, 1804–1825; d) H. Yan, Y. Lin, H. Wu, W. Zhang, Z. Sun, H. Cheng, W. Liu, C. Wang, J. Li, X. Huang, T. Yao, J. Yang, S. Wei, J. Lu, *Nat. Commun.* **2017**, *8*, 1070; e) H. Wang, X.-K. Gu, X. Zheng, H. Pan, J. Zhu, S. Chen, L. Cao, W.-X. Li, J. Lu, *Sci. Adv.* **2019**, *5*, eaat6413; f) H. Wang, C. Wang, H. Yan, H. Yi, J. Lu, *J. Catal.* **2015**, *324*, 59–68.

[16] Y. Deng, A. D. Handoko, Y. Du, S. Xi, B. S. Yeo, *ACS Catal.* **2016**, *6*, 2473–2481.

[17] a) M. Šćepanović, M. Grujić-Brojčin, K. Vojisavljević, S. Bernik, T. Srećković, *J. Raman Spectrosc.* **2010**, *41*, 914–921; b) Y. Wang, X. Zhan, F. Wang, Q. Wang, M. Safdar, J. He, *J. Mater. Chem. A* **2014**, *2*, 18413–18419; c) T. M. Khan, T. Bibi, B. Hussain, *Bull. Mater. Sci.* **2015**, *38*, 1851–1858.

[18] A. Dadlani, S. Acharya, O. Trejo, D. Nordlund, M. Peron, J. Razavi, F. Berto, F. B. Prinz, J. Torgersen, *ACS Appl. Mater. Interfaces* **2017**, *9*, 39105–39109.

[19] a) O. Hinrichsen, T. Genger, M. Muhler, *Chem. Eng. Technol.* **2000**, *23*, 956–959; b) M. B. Fichtl, J. Schumann, I. Kasatkin, N. Jacobsen, M. Behrens, R. Schlögl, M. Muhler, O. Hinrichsen, *Angew. Chem. Int. Ed.* **2014**, *53*, 7043–7047; *Angew. Chem.* **2014**, *126*, 7163–7167.

[20] a) A. Karelovic, P. Ruiz, *Catal. Sci. Technol.* **2015**, *5*, 869–881; b) I. Kasatkin, P. Kurr, B. Kniep, A. Trunschke, R. Schlögl, *Angew. Chem. Int. Ed.* **2007**, *46*, 7324–7327; *Angew. Chem.* **2007**, *119*, 7465–7468.

[21] a) H. S. Hsu, J. C. A. Huang, Y. H. Huang, Y. F. Liao, M. Z. Lin, C. H. Lee, J. F. Lee, S. F. Chen, L. Y. Lai, C. P. Liu, *Appl. Phys. Lett.* **2006**, *88*, 242507; b) D. A. McKeown, *Phys. Rev. B* **1992**, *45*, 2648–2653; c) A. Beck, M. Zabilskiy, M. A. Newton, O. Safonova, J. Bokhoven, *Nat. Catal.* **2021**, *4*, 488–497; d) A. Beck, M. A. Newton, M. Zabilskiy, P. Rzepka, M. G. Willinger, J. A. van Bokhoven, *Angew. Chem. Int. Ed.* **2022**, *61*, e202200301; *Angew. Chem.* **2022**, *134*, e202200301.

[22] a) D. Grandjean, V. Pelipenko, E. D. Batyrev, J. C. van den Heuvel, A. A. Khassin, T. M. Yurieva, B. M. Weckhuysen, *J. Phys. Chem. C* **2011**, *115*, 20175–20191; b) E. Frei, A. Gaur, H. Lichtenberg, L. Zwiener, M. Scherzer, F. Girgsdies, T. Lunkenbein, R. Schlögl, *ChemCatChem* **2020**, *12*, 4029–4033; c) M. Zabilskiy, V. L. Sushkevich, M. A. Newton, J. A. van Bokhoven, *ACS Catal.* **2020**, *10*, 14240–14244; d) G. Dennis, K. Konstantin, S. Ilya, G. Wolfgang, *ChemCatChem* **2017**, *9*, 365–372.

[23] F. Claeyssens, C. L. Freeman, N. L. Allan, Y. Sun, M. N. R. Ashfold, J. H. Harding, *J. Mater. Chem.* **2005**, *15*, 139–148.

[24] L. Grabow, M. Mavrikakis, *ACS Catal.* **2011**, *1*, 365–384.

[25] F. Studt, M. Behrens, E. L. Kunkes, N. Thomas, S. Zander, A. Tarasov, J. Schumann, E. Frei, J. B. Varley, F. Abild-Pedersen, J. K. Nørskov, R. Schlögl, *ChemCatChem* **2015**, *7*, 1105–1111.

[26] a) T. Reichenbach, K. Mondal, M. Jäger, T. Vent-Schmidt, D. Himmel, V. Dybbert, A. Bruix, I. Krossing, M. Walter, M. Moseler, *J. Catal.* **2018**, *360*, 168–174; b) T. Reichenbach, M. Walter, M. Moseler, B. Hammer, A. Bruix, *J. Phys. Chem. C* **2019**, *123*, 30903–30916; c) K. Mondal, A. Megha, A. Banerjee, M. Fortunelli, M. Walter, M. Moseler, *J. Phys. Chem. C* **2022**, *126*, 764–771.

[27] S. Bailey, G. F. Froment, J. W. Snoeck, K. C. Waugh, *Catal. Lett.* **1995**, *30*, 99–111.

Manuscript received: February 11, 2022
Accepted manuscript online: March 23, 2022
Version of record online: April 6, 2022